SCIENCE CHINA
Information Sciences

• RESEARCH PAPER •

January 2024, Vol. 67, Iss. 1, 112402:1–112402:7
https://doi.org/10.1007/s11432-022-3677-7

Radiation build-up and dissipation in Raman random fiber laser

Shengtao LIN[1], Zinan WANG[1*], Jiaojiao ZHANG[1], Pan WANG[1], Han WU[2] & Yifei QI[1]

[1]*Key Laboratory of Optical Fiber Sensing and Communications, University of Electronic Science and Technology of China, Chengdu* 611731*, China;*
[2]*College of Electronics and Information Engineering, Sichuan University, Chengdu* 610064*, China*

Received 26 August 2022/Revised 24 October 2022/Accepted 4 January 2023/Published online 27 November 2023

Abstract Raman random fiber laser (RRFL) is a complex physical system that arises from the distributed Raman amplification and the intrinsic stochasticity of fiber scattering. The analysis of the underlying lightwave kinetics at steady state has been the focus of considerable interest. However, the transient state, such as the RRFL build-up and dissipation, is particularly important for revealing the lightwave interaction process. Here, we investigate for the first time the RRFL dynamics at the transient state and track the RRFL temporal and spectral evolution theoretically and experimentally. Particularly, with the contribution of random distributed feedback, RRFL build-up exhibits continuous Verhulst logistic growth curves without cavity-related features, which is significantly different from the step-like growth curve of conventional fiber lasers. Furthermore, the radiation build-up duration is inversely related to the pump power, and the spectral evolution of the RRFL undergoes two phases, i.e., from spectral density increase to spectral broadening. From the steady state to the pump switch-off state, the RRFL output power dissipates immediately, and the remaining Stokes lightwave from the Rayleigh scattering will gradually disappear after one round trip. This work provides new insights into the transient dynamic features of the RRFL.

Keywords random fiber laser, stimulated Raman scattering, transient phenomenon, nonlinear optics, biological growth dynamics

1 Introduction

Raman random fiber laser (RRFL), generated from random distributed feedback in an amplified fiber waveguide medium [1], exhibits excellent performance with high efficiency [2], good beam quality [3], and wavelength agility [4]. RRFL has been widely used in optical fiber sensing and optical imaging [5, 6], and has recently attracted considerable attention in a high-power laser driver facility [7]. RRFL also involves complex lightwave propagation and interaction processes with random media presenting distinctive statistical properties [8] and has become a statistical platform to examine some challenging aspects of complex systems [9].

When operating at the steady state, RRFL exhibits a complex lasing process [5, 10, 11]. For the intensity fluctuations at the steady state, RRFL shows universal statistical properties, i.e., Gaussian distribution at the prelasing regime, Lévy behavior around the threshold, and Gaussian pattern above the threshold [8, 12]. Moreover, the turbulence [13] and optical rogue wave [14] behavior can be observed in RRFL, which contains a complex interplay process. For the spectrum statistics at the steady state, the nonlinear correlation between different parts of the RRFL spectra is observed through mutual information analysis [15], and the underlying stimulated Brillouin scattering is revealed. Furthermore, the transition from the paramagnetic phase to the spin glass phase in disordered magnetic systems can be observed in the RRFL platform using the Parisi overlap parameter [16–18]. In addition to the RRFL, the dynamic properties at the steady state have been investigated in other laser systems, including resonant-cavity-based fiber lasers [19, 20] and Brillouin random fiber laser [21].

* Corresponding author (email: znwang@uestc.edu.cn)

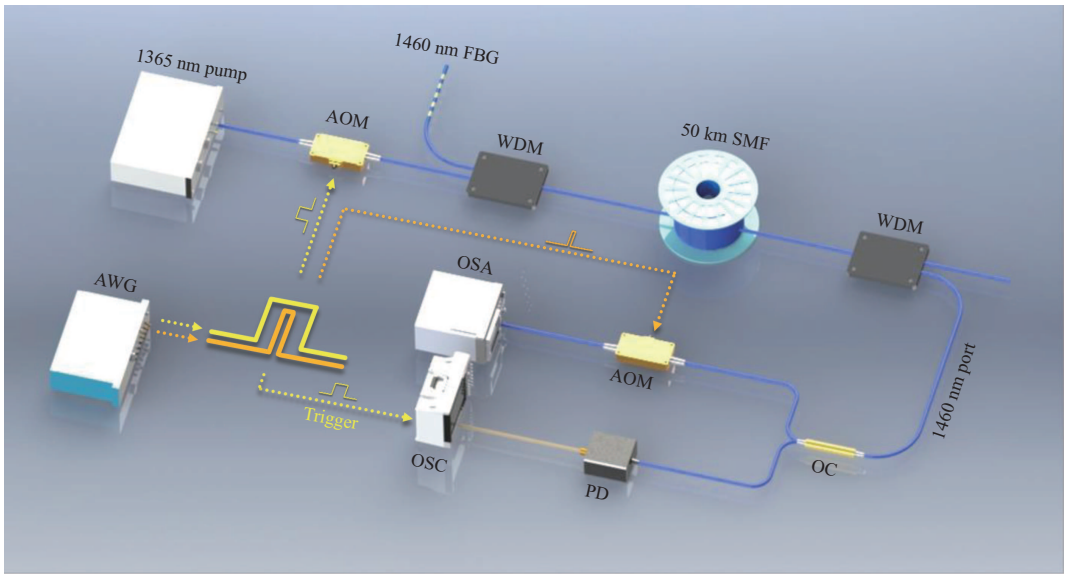

Figure 1 (Color online) Experimental setup for investigating RRFL transient state. OC: optical coupler; PD: photodetector; AWG: arbitrary waveform generator.

For the transient state, such as the radiation build-up and dissipation processes, it is difficult to synchronize and fast-track the evolution of the RRFL intensity and spectrum because of the continuous and broadband characteristics of the RRFL lightwave [19]. To the best of our knowledge, no research on the RRFL transient state has been conducted. However, the analysis of the build-up and dissipation processes of a complex physical system is critical to the investigation of the underlying physical mechanism. For instance, covert transient coherent multi-soliton states can be explored at the dissipative soliton transient region [22], the underlying seven different ultrafast phases are detected in the harmonic mode-locking build-up process [23], and the transient interference dynamics can be observed in the femtosecond mode-locking build-up process [24].

In this study, the transient state of the RRFL is characterized for the first time, and the experimental results are well consistent with the simulation results calculated by the generalized nonlinear Schrödinger equations. In the build-up region, the output power of the RRFL increases continuously and fits well with the Verhulst logistic model that is widely analyzed in biological growth dynamics, and the build-up duration is inversely related to the pump power. Moreover, the spectral evolution of the RRFL build-up is measured by chopping different RRFL stages using acousto-optic modulators (AOMs), and we observe that it undergoes two phases, i.e., from spectral density increase to spectral broadening. In the RRFL dissipation region, the generated Stokes laser dissipates immediately after switching off the pump power with a high extinction ratio, and the remaining Stokes lightwave will radiate out of the fiber after one round trip. Our investigations pave the way to understanding the RRFL lightwave kinetics at the transient state.

2 Methods

2.1 Experimental setup

The transient region of the RRFL is investigated based on a forward-pumped RRFL, as illustrated in Figure 1. The RRFL is pumped by a 1365 nm Raman fiber laser and the switching of the pump is controlled by the first fiber AOM (AOM1) with 2.3 dB insertion loss and 55 dB extinction ratio. The rise/fall time of the 1365 nm pump power, including electrical delay and AOM delay, is around 1 μs. The modulated pump is injected into a 50 km single mode fiber (SMF) through a 1365 nm/1460 nm wavelength division multiplexer (WDM), and the 1460 nm port is connected to a 1460 nm fiber Bragg grating (FBG) playing the role of point reflector. The generated RRFL outputs at the end of the fiber, and is separated from the pump by an additional 1365 nm/1460 nm WDM.

The temporal evolution of the RRFL is detected by a 10 MHz photoreceiver and sampled by an

Table 1 Parameters set in the simulation

Parameter	Pump	Stokes
λ	1365 nm	1460 nm
v_g	2.0509×10^8 m $\cdot$ s^{-1}	2.0504×10^8 m $\cdot$ s^{-1}
α	0.30 dB $\cdot$ km^{-1}	0.23 dB $\cdot$ km^{-1}
Gain	5.3×10^{-4} m$^{-1} \cdot$ W^{-1}	–
ε	1×10^{-7} m^{-1}	0.6×10^{-7} m^{-1}
γ	0.0018 m$^{-1} \cdot$ W^{-1}	0.0015 m$^{-1} \cdot$ W^{-1}
β_2	8.3011×10^{-27} s$^2 \cdot$ m^{-1}	1.7972×10^{-26} s$^2 \cdot$ m^{-1}
R_R	4×10^{-5}	4×10^{-5}
R_L	4×10^{-5}	0.99

oscilloscope (OSC) at a 20 MSa/s sampling rate. For the spectral evolution of RRFL, it is measured based on the time-slicing method [25], and a second fiber AOM (AOM2) is used in the scheme to realize 0.15 ms optical gate window that is shorter than the optical round-trip time. By varying the delay time between two AOMs' drive signals, we can record RRFL spectral properties in arbitrary states by an optical spectrum analyzer (OSA, YOKOGAWA AQ6370D in this work).

2.2 Simulation model

Based on the experimental setup, we also performed corresponding simulations to theoretically analyze the RRFL transient state, including RRFL build-up and dissipation. The simulation model is based on the generalized nonlinear Schrödinger equations (NLSEs) that can well describe the spectral and temporal dynamics of RRFL [26],

$$\frac{\partial u_p^{\pm}}{\partial z} \mp \frac{1}{v_{gs}} \frac{\partial u_p^{\pm}}{\partial t} \pm i\frac{\beta_{2p}}{2} \frac{\partial^2 u_p^{\pm}}{\partial t^2} \pm \frac{\alpha_p}{2} u_p^{\pm} = \pm i\gamma_p \left|u_p^{\pm}\right|^2 u_p^{\pm} \mp \frac{g_p(\omega)}{2} \left(\left\langle \left|u_s^{\pm}\right|^2 \right\rangle + \left\langle \left|u_s^{\mp}\right|^2 \right\rangle\right) u_p^{\pm}, \tag{1}$$

$$\frac{\partial u_s^{\pm}}{\partial z} \pm i\frac{\beta_{2s}}{2} \frac{\partial^2 u_s^{\pm}}{\partial t^2} \pm \frac{\alpha_s}{2} u_s^{\pm} \mp \frac{\varepsilon(\omega)}{2} u_s^{\mp} = \pm i\gamma_s \left|u_s^{\pm}\right|^2 u_s^{\pm} \pm \frac{g_s(\omega)}{2} \left(\left\langle \left|u_p^{\pm}\right|^2 \right\rangle + \left\langle \left|u_p^{\mp}\right|^2 \right\rangle\right) u_s^{\pm}, \tag{2}$$

where u is the complex envelope of the lightwave; 'p' and 's' represent the pump and Stokes waves, respectively; '+' and '−' are the forward and backward propagating waves, respectively; v_{gs} is the inverse group velocities between the pump and Stokes waves; ω is the angular frequency of lightwave; α, γ, β_2, ε, and g are the linear fiber loss, Kerr coefficient, second-order dispersion, Rayleigh scattering, and Raman gain, respectively. They are calculated and experimental measured in [27, 28]. The total length of the fiber is defined as L.

In addition, the boundary conditions are $P_p^+(0,\omega,t) = P_{in}(\omega) T_{Lp} + R_{Lp}(\omega) P_p^-(0,\omega,t)$, $P_p^-(L,\omega,t) = R_{Rp}(\omega) P_p^+(L,\omega,t)$, $P_s^+(0,\omega,t) = R_{Ls}(\omega) P_s^-(0,\omega,t)$, and $P_s^-(L,\omega,t) = R_{Rs}(\omega) P_s^+(L,\omega,t)$, where $R_L(\omega)$ and $R_R(\omega)$ are wavelength-dependent reflectivity at left and right fiber ends, respectively, and T_L is the corresponding transmittance. In addition, the value of $R_{Ls}(\omega)$ is experimentally measured with 0.2 nm bandwidth and 99% reflectivity. Other parameter values in the simulation are summarized in Table 1. The simulation is iterated by the split-step Fourier method [29], and the time-consuming Fourier transform process is performed in the graphics processing unit (GPU) using compute unified device architecture (CUDA) to speed up the computation.

Figure 2 shows the output Stokes power at the fiber end as a function of the pump power. The threshold of RRFL is about 0.72 W in the experimental results. Above the threshold, the power of the Stokes laser increases rapidly, and its slope efficiency gradually slows down toward a specific value. The changes in slope efficiency are caused by the shape of the Stokes power distribution in the fiber [30]. In addition, it can be found that the simulation results are in accordance with the experimental results, validating the effectiveness of our simulation.

3 Results and discussion

Here, the transient state of the RRFL during the build-up process is first investigated. Figure 3 shows the temporal and spectral evolution of the RRFL when the pump power is suddenly switched on. Figures 3(a), (b), (d), (e), (g), and (h) show the experimental results, and Figures 3(c), (f) and (i) show the corresponding simulation results.

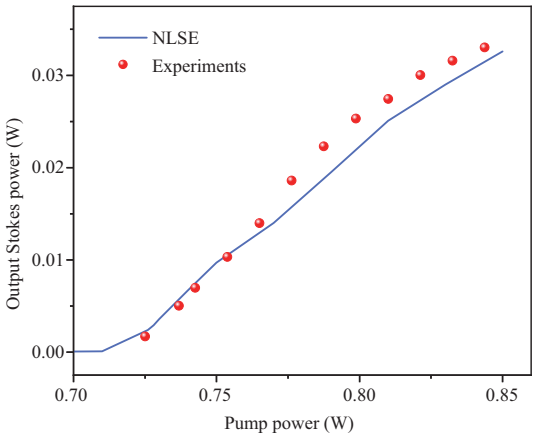

Figure 2 (Color online) Output power of the RRFL versus pump power (red dots: experimental data; solid line: numerical simulation results based on the NLSE model).

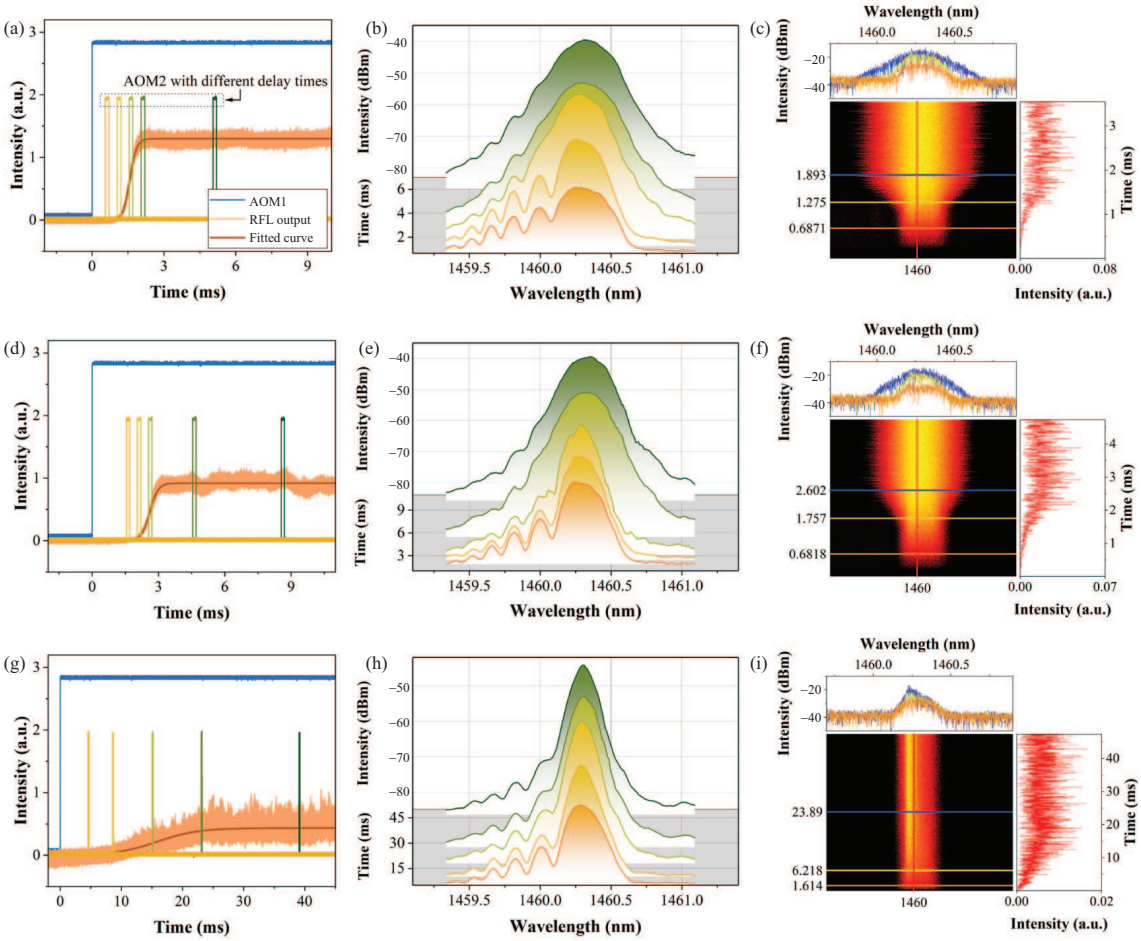

Figure 3 (Color online) Temporal and spectral evolution of the RRFL. (a)–(c) Well above the threshold; (d)–(f) above the threshold; (g)–(i) around the threshold. (a), (d), and (g) Temporal evolution in the experiment; (b), (e), and (h) spectral evolution in the experiment; (c), (f), and (i) temporal and spectral evolution in the simulation.

For the RRFL well above the threshold (0.85 W pump), the temporal characteristics are depicted in Figure 3(a). The pump is switched on by the trigger signal of AOM1, and the output power of the generated Stokes lightwave increases continuously without discrete steps determined by the cavity round-trip time [25]. The corresponding build-up time is approximately 2 ms, requiring only four optical round-trip times. The simulated temporal results shown in the red line spectral slice in Figure 3(c) are

consistent with the experimental results. Notably, the delay of the RRFL pump with the electrical trigger is approximately 1.5 ms, which is three orders of magnitude less than the RRFL build-up time; i.e., the blue trigger signal in Figure 3(a) can be used to reflect the operating status of the pump. Moreover, within 1 ms after switching on the pump, Stokes photons from the amplified spontaneous emission noise gradually accumulate. However, at this region, the Stokes power remains too weak to be detected by the photodetector, and the Stokes power increases exponentially, as indicated by the simulation results shown in Figure 3(c).

The spectral evolution of the RRFL is measured based on the time-slicing method, and the results are illustrated in Figure 3(b). By varying the delay time between trigger signals of two AOMs, we extracted five typical time slices in Figure 3(a), covering some typical stages from the RRFL build-up to the steady state. The line colors in Figure 3(b) are consistent with the time slices extracted in Figure 3(a). The spectral evolution undergoes two stages, which can be observed in detail in the simulation (Figure 3(c)). Initially, as the Stokes power increases, the spectral density increases rapidly, and the spectral bandwidth tends to narrow (from the orange line time slice to the yellow line time slice in Figure 3(c)). A further increase in spectral density gradually induces the effect of the Kerr nonlinear, resulting in RRFL broadening (from the yellow line time slice to the blue line time slice in Figure 3(c)).

Figures 3(d)–(f) and (g)–(i) show the evolution of the RRFL above and around the threshold with 0.8 and 0.73 W pump power, respectively. For the RRFL above the threshold, the evolution of the RRFL is consistent with the phenomenon well above the threshold, but the laser build-up time is longer, with approximately 4 ms corresponding to the eight optical round-trip times. For the RRFL around the threshold, the spectral broadening stage is not evident because the lower laser power is insufficient to induce significant Kerr effects. The build-up time for the RRFL around the threshold increases dramatically to 20 ms, and the higher noise floor compared with Figures 3(a) and (d) is caused by the larger gain chosen in the photoreceiver.

Notably, regardless of the pump power, the growth curve of the Stokes laser is continuous, indicating that the random distributed feedback of the Rayleigh scattering plays an important role in the generation of the RRFL. However, for the conventional Raman fiber lasers, the laser is generated from the resonance of the cavity; thus, the growth curve is stepwise in relation to the fiber cavity length [25], which is completely different from the RRFL.

Furthermore, the kinetics of the RRFL can be analogized to population dynamics in biology: Stokes photons are "predators" and pump photons are "prey". More "predators" will lead to fewer pump photons. Conversely, more "prey" will lead to more Stokes photons. The numbers of Stokes and pump photons will eventually reach equilibrium. The Verhulst logistic growth curve is a typical biological growth model that is used to characterize the dynamics of a stable population [31]. Thus, the curve is suitable for describing the growth process of the RRFL with stable output, and it can be expressed as

$$P_{\mathrm{Sout}}(t) = \frac{P_0 P_{\max}}{P_0 + (P_{\max} - P_0)G^{-t}}, \tag{3}$$

where P_{Sout} is the Stokes output power, P_0 is the initial noise from the amplifier spontaneous emission, $P_{\max}$ is the maximum output power, and G is the growth rate of the Stokes power. As illustrated in Figures 3(a), (d), and (g), the profile of the RRFL power growth fits well with Verhulst logistic growth model. The RRFL growth rate G well above the threshold is as high as 1030 $\mathrm{V \cdot s^{-1}}$, decreases to 226 $\mathrm{V \cdot s^{-1}}$ above the threshold, and is even as low as 1.3 $\mathrm{V \cdot s^{-1}}$ at the threshold. By varying the pump power, we can use RRFL to analyze biological population dynamics with different growth rates. Perhaps, further using the higher-order RRFL or utilizing the self-pulse effects [30,32], the RRFL could be used to investigate the multispecies growth characteristics and population dynamic competition in biology [33]. In this manner, the RRFL-based system may open up new important avenues for understanding more biological phenomena.

At the threshold, the RRFL exhibits extremely complex physical processes, including a sudden narrowing of the laser linewidth [34], Lévy statistical behavior [8], and ultra-narrow spectral mode dynamics [10]. Here, by varying the pump power in the simulation, we find that the build-up time of the RRFL starts up abruptly around the threshold from 3 ms (i.e., the build-up time of amplifier spontaneous emission) to 30 ms, as illustrated in Figure 4. Above the threshold, the build-up time of the RRFL is inversely related to the Stokes output power. With a further increase in the pump power, the Stokes build-up time gradually decreases to 10 ms at 0.01 W output power and 2 ms at 0.03 W output power. The numerical results are consistent with the experimental results. The slight deviation at the lower output power region

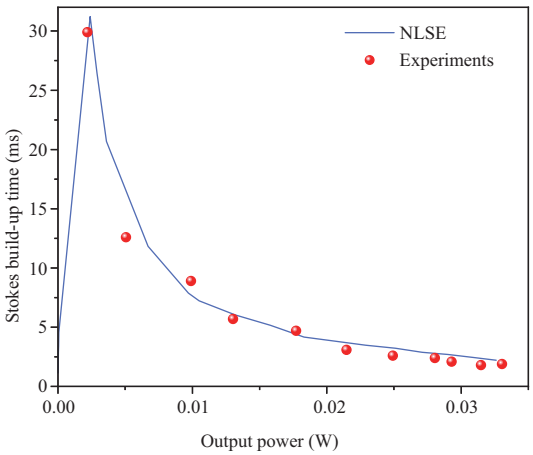

Figure 4 (Color online) Build-up time of the forward-pumped RRFL at different output Stokes powers.

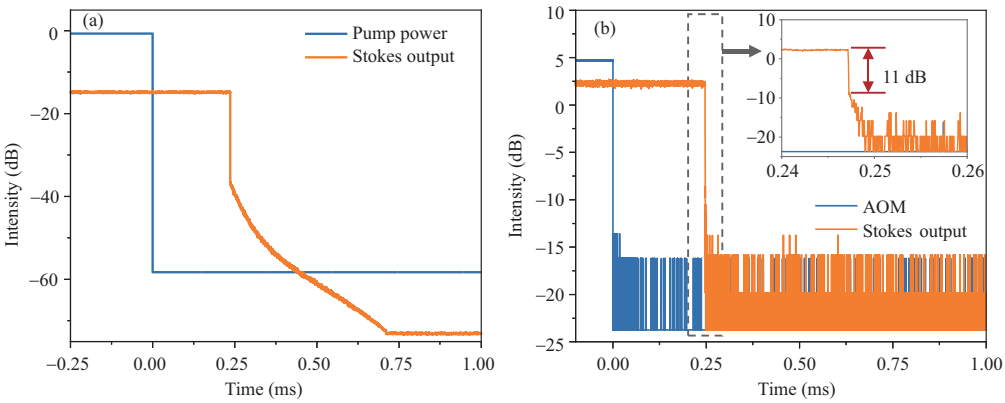

Figure 5 (Color online) Temporal evolution of the RRFL after switching off the pump. (a) Simulation results; (b) experimental results.

is mainly caused by the measurement uncertainty of the photodetector for signals with low signal-to-noise ratios. Notably, the results shown in Figure 4 are important for RRFL point sensing [28, 35]. When the center wavelength of the fiber Bragg grating sensor shifts because of external disturbance, it takes time to reestablish the RRFL to deliver the sensing information, which limits the RRFL sensing bandwidth. The duration from the pump switch-on state to the steady state in this work is the longest laser reestablish time that determines the lower bound of the sensing bandwidth. Thus, based on the results shown in Figure 4, we can appropriately increase the pump power to enhance the sensing bandwidth.

The transient state of the RRFL during the pump switch-off state is also investigated. The corresponding simulation is performed first. After the RRFL is well established, the pump power is set to 0, retaining noise in the fiber. At this moment, the generated Stokes laser will drop off suddenly after half of the round-trip time, exhibiting a high sensitivity to the pump power. Moreover, the remaining Stokes lightwave from the previous Rayleigh scattering will radiate out of the fiber within one round trip, as shown in Figure 5(a). Figure 5(b) shows the experimental results after switching off the pump, and the pump power is controlled by the trigger signal of AOM1. The drop-off phenomenon is consistent with the simulation results, showing a sharp falling edge (i.e., less than 0.1 μs) and a high extinction ratio (i.e., ∼11 dB). Then, the Stokes power will further decay exponentially. The decay process is recorded in several microseconds, which is longer than the rise/fall time of the photoreceiver (i.e., ∼80 ns). Afterward, the Stokes signal will be obscured in the measured noise.

4 Conclusion

In this work, we analyze the transient state of the RRFL for the first time. In the RRFL build-up region, the temporal evolution of the RRFL shows Verhulst logistic growth curves, and the build-up

time is inversely related to the pump power. Furthermore, the spectral evolution of the RRFL contains two stages, i.e., from spectral density increase to spectral broadening. By contrast, after switching off the pump, the generated Stokes laser dissipates immediately, and the remaining Stokes lightwave will gradually radiate out of the fiber. This work provides new insights into the underlying complex physics of the RRFL dynamics, and the results will be beneficial for research on other complex systems, such as biological dynamics and rogue wave build-up.

Acknowledgements This work was supported by National Natural Science Foundation of China (Grant No. 62075030), National Ten-Thousand Talent Program (Grant No. W030211001001), and Sichuan Provincial Project for Outstanding Young Scholars in Science and Technology (Grant No. 2020JDJQ0024). The authors would like to thank Prof. Sergei Turitsyn from Aston University for the helpful discussions.

References

1 Turitsyn S K, Babin S A, El-Taher A E, et al. Random distributed feedback fibre laser. Nat Photon, 2010, 4: 231–235
2 Wang Z N, Wu H, Fan M Q, et al. High power random fiber laser with short cavity length: theoretical and experimental investigations. IEEE J Sel Top Quantum Electron, 2015, 21: 10–15
3 Xu J, Huang L, Jiang M, et al. Near-diffraction-limited linearly polarized narrow-linewidth random fiber laser with record kilowatt output. Photon Res, 2017, 5: 350
4 Zhang L, Jiang H, Yang X, et al. Nearly-octave wavelength tuning of a continuous wave fiber laser. Sci Rep, 2017, 7: 42611
5 Churkin D V, Sugavanam S, Vatnik I D, et al. Recent advances in fundamentals and applications of random fiber lasers. Adv Opt Photon, 2015, 7: 516
6 Wang S, Zhang W, Yang N, et al. High-power multimode random fiber laser for speckle-free imaging. Annalen der Physik, 2021, 533: 2100390
7 Fan M, Lin S, Wu H, et al. Research progress of random fiber lasers' characteristics in time-frequency-spatial domain. High Power Laser and Particle Beams, 2021, 33: 111003
8 Li J, Wu H, Wang Z, et al. Lévy spectral intensity statistics in a Raman random fiber laser. Opt Lett, 2019, 44: 2799
9 Gomes A S L, de Araújo C B, Mac do A M S, et al. Photonics bridges between turbulence and spin glass phenomena in the 2021 Nobel Prize in Physics. Light Sci Appl, 2022, 11: 104
10 Kirik A E, Vatnik I D, Churkin D V. Direct measurements of localized spectral modes in random distributed feedback fiber laser. Results Phys, 2021, 28: 104651
11 Gorbunov O A, Sugavanam S, Vatnik I D, et al. Poisson distribution of extreme events in radiation of random distributed feedback fiber laser. Opt Lett, 2020, 45: 2375
12 Lima B C, Gomes A S L, Pincheira P I R, et al. Observation of Lévy statistics in one-dimensional erbium-based random fiber laser. J Opt Soc Am B, 2017, 34: 293
13 González I R, Lima B C, Pincheira P I, et al. Turbulence hierarchy in a random fibre laser. Nature Commun, 2017, 8: 8–15
14 Xu J, Wu J, Ye J, et al. Optical rogue wave in random fiber laser. Photon Res, 2020, 8: 1
15 Sugavanam S, Sorokina M, Churkin D V. Spectral correlations in a random distributed feedback fibre laser. Nat Commun, 2017, 8: 1–8
16 Gomes A S L, Lima B C, Pincheira P I R, et al. Glassy behavior in a one-dimensional continuous-wave erbium-doped random fiber laser. Phys Rev A, 2016, 94: 011801
17 González I R R, Raposo E P, Macêdo A M S, et al. Coexistence of turbulence-like and glassy behaviours in a photonic system. Sci Rep, 2018, 8: 17046
18 Zhou Z, Chen L, Bao X. High efficiency Brillouin random fiber laser with replica symmetry breaking enabled by random fiber grating. Opt Express, 2021, 29: 6532
19 Sugavanam S, Fabbri S, Le S T, et al. Real-time high-resolution heterodyne-based measurements of spectral dynamics in fibre lasers. Sci Rep, 2016, 6: 23152
20 Aragoneses A, Carpi L, Tarasov N, et al. Unveiling temporal correlations characteristic of a phase transition in the output intensity of a fiber laser. Phys Rev Lett, 2016, 116: 033902
21 Zhang L, Qiu Z, Xiao Z, et al. Frequency-stabilized Brillouin random fiber laser enabled by self-inscribed transient population grating. Opt Lett, 2022, 47: 150
22 Ryczkowski P, Närhi M, Billet C, et al. Real-time full-field characterization of transient dissipative soliton dynamics in a mode-locked laser. Nat Photon, 2018, 12: 221–227
23 Liu X, Pang M. Revealing the buildup dynamics of harmonic mode-locking states in ultrafast lasers. Laser Photonics Rev, 2019, 13: 1800333
24 Herink G, Jalali B, Ropers C, et al. Resolving the build-up of femtosecond mode-locking with single-shot spectroscopy at 90 MHz frame rate. Nat Photon, 2016, 10: 321–326
25 Suret P, Walczak P, Randoux S. Transient buildup of the optical power spectrum in Raman fiber lasers. Opt Express, 2013, 21: 2331
26 Smirnov S V, Churkin D V. Modeling of spectral and statistical properties of a random distributed feedback fiber laser. Opt Express, 2013, 21: 21236
27 Lin S, Wang Z, Li J, et al. Nonlinear dynamics of four-wave mixing, cascaded stimulated Raman scattering and self Q-switching in a common-cavity ytterbium/Raman random fiber laser. Optics Laser Tech, 2021, 134: 106613
28 Lin S, Wang Z, Qi Y, et al. Wideband remote-sensing based on random fiber laser. J Lightwave Technol, 2022, 40: 3104–3110
29 Agrawal G P. Nonlinear Fiber Optics. 4th ed. Pittsburgh: Academic Press, 2006
30 Lin S, Wang Z, Araújo H A, et al. Ultrafast convergent power-balance model for Raman random fiber laser with half-open cavity. Opt Express, 2020, 28: 22500–22510
31 Tsoularis A, Wallace J. Analysis of logistic growth models. Math Biosci, 2002, 179: 21–55
32 Xu J, Ye J, Liu W, et al. Passively spatiotemporal gain-modulation-induced stable pulsing operation of a random fiber laser. Photon Res, 2017, 5: 598
33 Chesson P. Multispecies competition in variable environments. Theor Population Biol, 1994, 45: 227–276
34 Kolokolov I V, Churkin D V, Vatnik I D, et al. Wave kinetics of random fibre lasers. Nature Commun, 2015, 2: 1–6
35 Wang Z N, Rao Y J, Wu H, et al. Long-distance fiber-optic point-sensing systems based on random fiber lasers. Opt Express, 2012, 20: 17695–17700